Hindawi
Quantum Engineering
Volume 2023, Article ID 6929253, 12 pages
https://doi.org/10.1155/2023/6929253

Research Article

Mid-infrared Spectrally Pure Single-Photon States Generation from 22 Nonlinear Optical Crystals

Wu-Hao Cai,[1,2,3] **Ying Tian**,[1] **and Rui-Bo Jin**[1]

[1]*Hubei Key Laboratory of Optical Information and Pattern Recognition, Wuhan Institute of Technology, Wuhan 430205, China*
[2]*Research Institute of Electrical Communication, Tohoku University, 2-1-1 Katahira, Sendai 980-8577, Japan*
[3]*Graduate School of Engineering, Tohoku University, 6-6 Aramaki Aza Aoba, Aoba-ku, Sendai 980-8579, Japan*

Correspondence should be addressed to Rui-Bo Jin; jin@wit.edu.cn

Received 24 March 2023; Revised 25 April 2023; Accepted 29 July 2023; Published 24 August 2023

Academic Editor: YuBo Sheng

Copyright © 2023 Wu-Hao Cai et al. This is an open access article distributed under the Creative Commons Attribution License, which permits unrestricted use, distribution, and reproduction in any medium, provided the original work is properly cited.

We theoretically investigate the preparation of pure-state single-photon source from 14 birefringent crystals (CMTC, THI, $LiIO_3$, AAS, HGS, CGA, TAS, AGS, AGSe, GaSe, LIS, LISe, LGS, and LGSe) and 8 periodic poling crystals (LT, LN, KTP, KN, $BaTiO_3$, $MgBaF_4$, PMN-0.38PT, and OP-ZnSe) in a wavelength range from 1224 nm to 11650 nm. The three kinds of group-velocity-matching (GVM) conditions, the phase-matching conditions, the spectral purity, and the Hong-Ou-Mandel interference are calculated for each crystal. This study may provide high-quality single-photon sources for quantum sensing, quantum imaging, and quantum communication applications at the mid-infrared wavelength range.

1. Introduction

Single-photon source at the mid-infrared (MIR) wavelength range (approximately 2–20 μm) has important potential applications in quantum sensing, quantum imaging, and quantum communication [1–4]. Firstly, the 3–5 μm band contains absorption peaks of many gases, such as H_2O, CO, CO_2, SO_2, and SO_3 [5], so this band is important for sensing of these gases in environmental monitoring [6, 7]; the 7–10 μm band contains absorption peaks of H_2, O_2, CH_4, O_3, trinitrotoluene (TNT), acetone, and sarin [5]. Therefore, this band is important for sensing chemical or explosive materials in the applications of industrial production or defense security. The single-photon source in these gas sensing applications may provide ultrahigh sensitivity [8]. Secondly, 3–5 μm and 8–14 μm are two widely used ranges for MIR thermal infrared imaging cameras for medical and forensic usage [9] since the room temperature objects emit light at these wavelength ranges. Also, MIR single-photon sources can provide a diagnosis in a noninvasive manner, which is important for medical or biological samples [10]. Thirdly, 3–5 μm is also an atmospheric transmission window with relatively high transparency, which is useful for large-scale free-space quantum communications, such as entanglement distribution [11], quantum key distribution [12], or quantum direct communication [13].

Spontaneous parametric down-conversion (SPDC) and four-wave mixing (FWM) are two widely used methods to prepare single photons. Many previous works have been dedicated to the development of high-quality single-photon sources or entangled photon sources in the MIR range from an SPDC or FWM process. On the experimental side, periodically poled lithium niobate (PPLN) [14–16], GaP [17], and silicon waveguide [18] have been investigated to prepare a single-photon source; PPLN [19] has been studied for entangled photon source generation. On the theory side, PPLN [20], periodically poled potassium niobate (PPKN) [21], $0.62Pb(Mg_{1/3}Nb_{2/3})O_3 - 0.38PbTiO_3$ (PMN-0.38PT) [22], etc. have been investigated for single-photon source [23–27]; p-doped semiconductor [28] has been studied for entangled photon source. In addition, some studies explored single-photon detection by superconducting nanowire single-photon detector (SNSPD) [29–31] or by silicon avalanche photodiode (SAPD) in an upconversion configuration [14, 32].

However, the previous studies are still insufficient for the need of MIR applications. On the one hand, the previous experimental work is mainly focused on PPLN crystal, and the wavelength range is below 5 μm. So, the range from 5 to 20 μm still needs further exploration. On the other hand, the spectrally pure single-photon source is proved to be a good resource [33], but this source is still rare because the group-velocity matching (GVM) conditions can only be matched at very limited wavelengths in a crystal. Therefore, it is still necessary to explore more nonlinear optical crystals to fully meet the need of MIR band applications. For this purpose, in this work, we investigate MIR spectrally pure single-photon generation from 14 crystals by the birefringence phase-matching (BPM) method and 8 crystals by the quasi-phase-matching (QPM) method. They can meet three kinds of GVM conditions and prepare spectrally uncorrelated biphotons so as to generate spectrally pure heralded single-photon states.

2. Theory

2.1. The Characteristics of 22 Kinds of Nonlinear Crystals. We investigate 22 kinds of nonlinear crystals in this work. Table 1 summarizes them from several perspectives, name, axial type, point group, transparency range, and the maximal nonlinear coefficient. We separate these crystals into three categories by their axial type or phase-matching form in order to illustrate the result more clearly in the next section. Most Sellmeier equations were obtained from references [34, 35], and we have updated some Sellmeier equations with the latest references and concluded them in Table 1.

In the first category, 9 birefringent uniaxial crystals are listed in the table. They have a very large transparency range up to 20 μm except for CMTC and $LiIO_3$. We show 4 birefringent biaxial crystals in the second category, and these four crystals can be written as LiMX (M = In, Ga and X = S, Se). Here, In and Ga are elements of group IIIA in the periodic table; S and Se are elements of group VIA. They are all mm2 point group. With their transparency range up to 14 μm, they have similar properties and can perform many applications in the MIR band. The other 8 periodic poling crystals usually realize their phase-matching by the QPM method, so we discuss them in Sections 3.2 and 4 in detail.

2.2. The GVM Theory of Spectrally Pure Single-Photon States Generation. The SPDC process generates the biphoton state $|\psi\rangle$, which can be written as follows:

$$|\psi\rangle = \int_0^\infty \int_0^\infty \mathrm{d}\omega_s \mathrm{d}\omega_i f(\omega_s, \omega_i) \hat{a}_s^\dagger(\omega_s) \hat{a}_i^\dagger(\omega_i) |0\rangle |0\rangle, \quad (1)$$

where $\hat{a}^\dagger$ is the creation operator, ω is the angular frequency, and the subscripts s and i denote the signal and idler photons. The joint spectral amplitude (JSA) $f(\omega_s, \omega_i)$ can be obtained by multiplying the pump envelope function (PEF) $\alpha(\omega_s, \omega_i)$ and the phase-matching function (PMF) $\phi(\omega_s, \omega_i)$, i.e., $f(\omega_s, \omega_i) = \alpha(\omega_s, \omega_i) \times \phi(\omega_s, \omega_i)$.

For PEF, it is usually a Gaussian distribution and can be expressed as follows [51]:

$$\alpha(\omega_s, \omega_i) = \exp\left[-\frac{1}{2}\left(\frac{\omega_s + \omega_i - \omega_{p0}}{\sigma_p}\right)^2\right], \quad (2)$$

where σ_p is the bandwidth of the pump, ω_{p0} is the center frequency of the pump, and the full-width at half-maximum (FWHM) is $\mathrm{FWHM}_\omega = 2\sqrt{\ln(2)}\sigma_p \approx 1.67\sigma_p$.

If we use wavelengths as the variable by $\omega = 2\pi c/\lambda$ for ease of calculation, the PEF can be rewritten as follows:

$$\alpha(\lambda_s, \lambda_i) = \exp\left\{-\frac{1}{2}\left(\frac{1/\lambda_s + 1/\lambda_i - 1/(\lambda_0/2)}{\Delta\lambda/\left[(\lambda_0/2)^2 - (\Delta\lambda/2)^2\right]}\right)\right\}, \quad (3)$$

where $\lambda_0/2$ is the central wavelength of the pump, $\Delta\lambda$ is the bandwidth of wavelength, and $\sigma_p = 2\pi c/\Delta\lambda/[(\lambda_0)^2 - (\Delta\lambda/2)^2]$, where c is the light speed.

For $\Delta\lambda \ll \lambda_0$, the FWHM of the pump at the intensity level is $\mathrm{FWHM}_\lambda \approx 2\sqrt{\ln(2)}\Delta\lambda \approx 1.67\Delta\lambda$.

By assuming a flat phase distribution, the PMF can be written as *sinc* function shape [51],

$$\phi(\omega_s, \omega_i) = \mathrm{sinc}\left(\frac{\Delta kL}{2}\right), \quad (4)$$

where L is the length of crystal and Δk is the wave vector mismatch. For QPM case, $\Delta k = k_p - k_i - k_s \pm 2\pi/\Lambda$ and $k = 2\pi n(\lambda)/\lambda$ is the wave vector. The refractive index $n(\lambda)$ is a function of wavelength λ. Λ is the poling period and $\Lambda = 2\pi/|k_p - k_i - k_s|$. For BPM case, $\Delta k = k_p - k_i - k_s$ and $k = 2\pi n(\lambda, \theta, \varphi)/\lambda$. For ordinary ray (o-ray), the refractive index $n_o(\lambda)$ is a function of wavelength λ. While for extraordinary ray (e-ray), the refractive index $n_e(\lambda, \theta, \varphi)$ is a function of polar angle θ, azimuth angle φ, and wavelength λ.

According to the refractive index coordinate in Appendix of reference [52], θ is the polar angle between the optical axis of the crystal and the light propagation direction and φ is the azimuth angle in the xy plane. For uniaxial crystals, θ is the cutting angle of the crystals. For biaxial crystals, when light propagates in the xz plane, $\varphi = 0^\circ$ and θ is the cutting angle; when light propagates in the yz plane, $\varphi = 90^\circ$ and θ is the cutting angle; when light propagates in the xy plane, $\theta = 90^\circ$ and φ is the cutting angle.

When $\Delta k = 0$, the phase-matching condition is satisfied. Under this precondition, we consider the GVM condition to prepare an intrinsic spectrally pure state. The angle θ_{PMF} between the positive direction of the horizontal axis and the ridge direction of the PEF is determined by [53] as follows:

$$\tan(\theta_{\mathrm{PMF}}) = -\left(\frac{V_{g,p}^{-1}(\omega_p) - V_{g,s}^{-1}(\omega_s)}{V_{g,p}^{-1}(\omega_p) - V_{g,i}^{-1}(\omega_i)}\right), \quad (5)$$

where $V_{g,\mu} = d\omega/dk_\mu(\omega) = 1/k_\mu'(\omega)$, $(\mu = p, s, i)$ is the group velocity of the pump, the signal, and the idler.

We consider three kinds of GVM conditions [54]. The GVM_1 condition ($\theta_{\mathrm{PMF}} = 0^\circ$) is as follows:

Table 1: Main properties of the 10 uniaxial birefringent crystals (part I), 4 biaxial birefringent crystals (part II), and 8 periodic poling crystals (part III) discussed in this work, including the chemical formula, the axis (uniaxial, biaxial, or isotropic), the point group, the transparency range $\lambda_{\text{transp.}}$, and the maximal nonlinear coefficient $d_{\max}$ at different wavelengths (in μm in the bracket). Most of the data were obtained from references [34, 35]. The $BaTiO_3$ crystal has different types of point group at different temperatures. $^{*}d_{+} = |d_{31}\sin\theta| + |d_{22}\cos\theta|$. † The calculated result is from [22] according to the method from [36].

Name (ref.)	Chemical formula	Axis	Point group	$\lambda_{transp.}$ (μm)	$d_{\max(\text{wavelength})}$ (pm/V)
CMTC	$CdHg(SCN)_4$	Uniaxial	$\bar{4}$	0.40 ~ 2.35	$d_{31(1.064)} = 6.2 \pm 1.2$
THI	Tl_4HgI_6	Uniaxial	4mm	1.00 ~ 60.0	Unknown
$LiIO_3$ [37]	$LiIO_3$	Uniaxial	6	0.28 ~ 6.00	$d_{33(1.064)} = 4.6 \pm 0.3$
AAS	Ag_3AsS_3	Uniaxial	3m	0.61 ~ 13.3	$d_{22(1.064)} = 16.6 \pm 2.5$
HGS [38]	$HgGa_2S_4$	Uniaxial	$\bar{4}$	0.55 ~ 13.0	$d_{36(1.064)} = 31.5 \pm 4.7$
CGA [39]	$CdGeAs_2$	Uniaxial	$\bar{4}2$m	2.30 ~ 18.0	$d_{36(10.6)} = 186 \pm 16$
TAS	Tl_3AsSe_3	Uniaxial	3m	1.28 ~ 17.0	$d_{+(10.6)} = 68 \pm 31$
AGS	$AgGaS_2$	Uniaxial	$\bar{4}2$m	0.47 ~ 13.0	$d_{36(10.6)} = 12.5 \pm 2.5$
AGSe	$AgGaSe_2$	Uniaxial	$\bar{4}2$m	0.71 ~ 19.0	$d_{36(10.591)} = 39.5 \pm 1.9$
GaSe [40]	GaSe	Uniaxial	$\bar{6}2$m	0.62 ~ 20.0	$d_{22(10.6)} = 54 \pm 11$ [40]
LIS [41]	$LiInS_2$	Biaxial	mm2	0.34 ~ 13.2	$d_{33(2.3)} = -16 \pm 4$
LISe [42]	$LiInSe_2$	Biaxial	mm2	0.46 ~ 14.0	$d_{31(2.3)} = -16 \pm 4$ [43]
LGS [44]	$LiGaS_2$	Biaxial	mm2	0.32 ~ 11.6	$d_{33(2.3)} = -10.7 \pm 2.7$ [45]
LGSe [46]	$LiGaSe_2$	Biaxial	mm2	0.37 ~ 13.2	$d_{33(2.3)} = -18.2 \pm 4.6$ [45]
LT [47]	$LiTaO_3$	Uniaxial	3m	0.28 ~ 5.50	$d_{33(1.064)} = 12.9$
LN	$LiNbO_3$	Uniaxial	3m	0.40 ~ 5.50	$d_{33(1.064)} = 25.2$
KTP	$KTiOPO_4$	Biaxial	mm2	0.35 ~ 4.50	$d_{33(1.064)} = 14.6 \pm 0.7$
KN	$KNbO_3$	Biaxial	mm2	0.40 ~ 4.50	$d_{11(1.064)} = 21.9 \pm 0.5$ [48]
$BaTiO_3$	$BaTiO_3$	Uniaxial	4mm (room temp.)	0.40 ~ 9.00	$d_{32(1.06)} = 14.4 \pm 2.5$
$MgBaF_4$	$MgBaF_4$	Biaxial	mm2	0.14 ~ 10.0	$d_{32(1.064)} = 0.039$
PMN-0.38PT [49]	$0.62Pb(Mg_{1/3}Nb_{2/3})O_3 - 0.38PbTiO_3$	Uniaxial	4mm	0.3 ~ 11.0	$^{\dagger}d_{33(1.064)} = 12.6$
OP-ZnSe [50]	ZnSe	Isotropic	$\bar{4}3$m	0.45 ~ 18.0	$d_{36(0.852)} = 53.8$

$$V_{g,p}^{-1}(\omega_p) = V_{g,s}^{-1}(\omega_s). \tag{6}$$

The GVM_2 condition ($\theta_{\text{PMF}} = 90^{\circ}$) is as follows:

$$V_{g,p}^{-1}(\omega_p) = V_{g,i}^{-1}(\omega_i). \tag{7}$$

The GVM_3 condition ($\theta_{\text{PMF}} = 45^{\circ}$) is as follows:

$$2V_{g,p}^{-1}(\omega_p) = V_{g,s}^{-1}(\omega_s) + V_{g,i}^{-1}(\omega_i). \tag{8}$$

The pure-state not only can be prepared through these three GVM conditions but also all the conditions that the θ_{PMF} angles are between 0 and 90° [55, 56]. Since these three GVM conditions are listed in equations (6)–(8), which are the most widely-used cases in the experiment, we mainly consider these three conditions within this work. Besides, the degenerate or nondegenerate case of other θ_{PMF} under type-II and type-0 phase-matching conditions will be illustrated in section 3.3.

Besides, it is important to discuss the calculation of spectral purity. The purity of JSA can be calculated through Schmidt decomposition on $f(\omega_s, \omega_i)$ [51] as follows:

$$f(\omega_s, \omega_i) = \sum_j c_j \phi_j(\omega_s)\varphi_j(\omega_i), \tag{9}$$

where $\phi_j(\omega_s)$ and $\varphi_j(\omega_i)$ are the two orthogonal basis vectors in the frequency domain and c_j is a set of non-negative real coefficients that satisfy the normalization condition $\sum_j c_j^2 = 1$. Then, the purity P can be defined as follows:

$$P \equiv \sum_j c_j^4. \tag{10}$$

3. Calculation and Simulation

3.1. Birefringent Crystals. Firstly, we consider the birefringent crystals with the BPM method. We assume that the wavelength has degenerated, i.e., $2\lambda_p = \lambda_s = \lambda_i$. For uniaxial crystals, negative uniaxial crystals satisfy the Type-II SPDC with $e \longrightarrow o + e$ phase-matching interaction. Here, the pump and idler are extraordinary (e) beams, while the signal is ordinary (o) beam. In contrast, the positive uniaxial crystals can meet the Type-II SPDC with $o \longrightarrow o + e$ phase-matching interaction. Note that all the simulations are based on collinear figuration.

Ten kinds of uniaxial crystals are investigated in this work. Taking AgSe crystal as an example, we plot the PMF and $GVM_{1(2,3)}$ conditions for different wavelengths and phase-matched angles in Figure 1(a). The PMF (red) crosses the $GVM_{1(2,3)}$ (blue and green) at three black points, which meet the PMF and three kinds of GVM conditions simultaneously. The three points are associated with wavelengths of 4,914, 8,158, and 6,272 nm, respectively, and angles of 79.9°, 81.9°, and 67.2°. Furthermore, we calculate the other uniaxial crystals with the same method, and then we summarize the result in Table 2. In Table 2, the down-converted photons have a wavelength range from 1,298 to 11,650 nm, which is in the near-infrared (NIR) and MIR

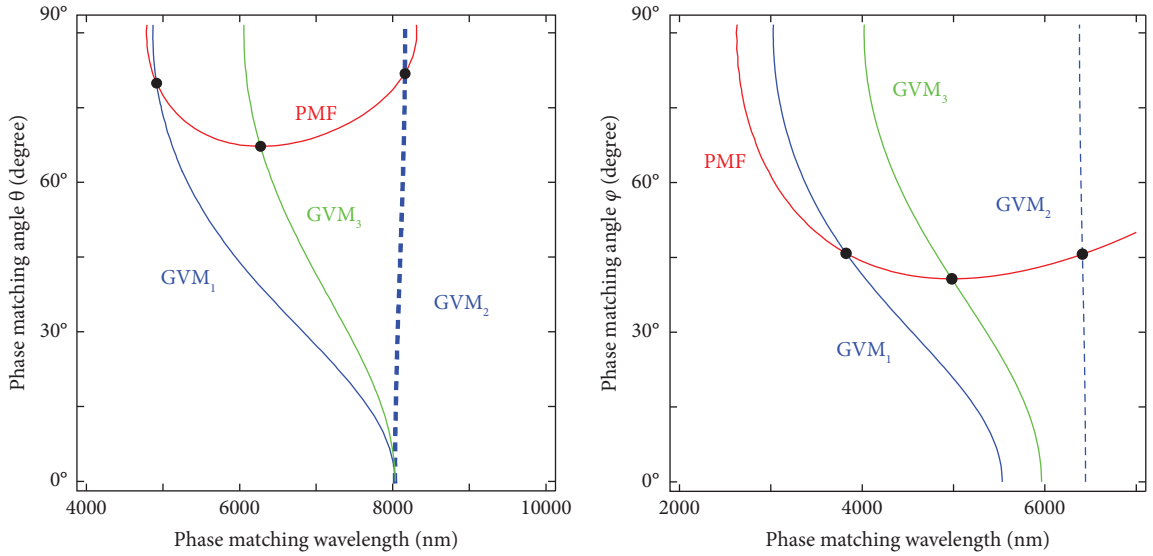

FIGURE 1: The phase-matching function and group-velocity matching functions ($GVM_{1(2,3)}$) for different signal/idler wavelength and phase-matching angle (polar angle) θ for AGSe crystal (a) and phase-matching (azimuth angle) angle φ for LISe crystal in the xy plane (b). In this calculation, we consider the type-II phase-matching condition with collinear and wavelength-degenerate ($2\lambda_p = \lambda_s = \lambda_i$) configuration.

TABLE 2: Three kinds of GVM conditions for 10 uniaxial BPM crystals. $\lambda_{p(s,i)}$ is the GVM wavelength for the pump (signal, idler). θ is the phase-matching angle, and d_{eff} is the effective nonlinear coefficient. The Sellmeier equations are obtained from references [34, 35]. Most of the d_{eff} values can be obtained from the SNLO *v*78 software package, developed by AS-Photonics, LLC [57]. *The d_{eff} value for CMTC is not available from SNLO, we have calculated d_{eff} using the method in the Appendix of reference [52] and considering Miller's rule [58]. † The d_{eff} value for THI is unknown.

Name	GVM_1 (purity ≈ 0.97)	GVM_2 (purity ≈ 0.97)	GVM_3 (purity ≈ 0.82)
CMTC*	$\lambda_p = 649$ nm, $\lambda_{s,i} = 1298$ nm $\theta = 41.2^\circ$, $d_{\text{eff}} = -4.46$ pm/V	$\lambda_p = 1156$ nm, $\lambda_{s,i} = 2312$ nm $\theta = 43.6^\circ$, $d_{\text{eff}} = -3.63$ pm/V	$\lambda_p = 829$ nm, $\lambda_{s,i} = 1658$ nm $\theta = 38.2^\circ$, $d_{\text{eff}} = -4.13$ pm/V
THI†	$\lambda_p = 2841$ nm, $\lambda_{s,i} = 5682$ nm $\theta = 29.3^\circ$, d_{eff} = unknown	$\lambda_p = 4822$ nm, $\lambda_{s,i} = 9644$ nm $\theta = 29.3^\circ$, d_{eff} = unknown	$\lambda_p = 3705$ nm, $\lambda_{s,i} = 7410$ nm $\theta = 27.2^\circ$, d_{eff} = unknown
$LiIO_3$	$\lambda_p = 835$ nm, $\lambda_{s,i} = 1670$ nm $\theta = 29.3^\circ$, $d_{\text{eff}} = 0.09$ pm/V	$\lambda_p = 1460$ nm, $\lambda_{s,i} = 2920$ nm $\theta = 29.7^\circ$, $d_{\text{eff}} = 0.09$ pm/V	$\lambda_p = 1088$ nm, $\lambda_{s,i} = 2176$ nm $\theta = 27.2^\circ$, $d_{\text{eff}} = 0.09$ pm/V
AAS	$\lambda_p = 2151$ nm, $\lambda_{s,i} = 4302$ nm $\theta = 22.3^\circ$, $d_{\text{eff}} = 0.16$ pm/V	$\lambda_p = 3617$ nm, $\lambda_{s,i} = 7234$ nm $\theta = 22.3^\circ$, $d_{\text{eff}} = 0.15$ pm/V	$\lambda_p = 2793$ nm, $\lambda_{s,i} = 5586$ nm $\theta = 20.7^\circ$, $d_{\text{eff}} = 0.16$ pm/V
HGS	$\lambda_p = 1704$ nm, $\lambda_{s,i} = 3408$ nm $\theta = 60.1^\circ$, $d_{\text{eff}} = 0.29$ pm/V	$\lambda_p = 2819$ nm, $\lambda_{s,i} = 5638$ nm $\theta = 59.8^\circ$, $d_{\text{eff}} = 0.29$ pm/V	$\lambda_p = 2206$ nm, $\lambda_{s,i} = 4412$ nm $\theta = 54.2^\circ$, $d_{\text{eff}} = 0.32$ pm/V
CGA	$\lambda_p = 3692$ nm, $\lambda_{s,i} = 7384$ nm $\theta = 54.6^\circ$, $d_{\text{eff}} = 0.02$ pm/V	$\lambda_p = 5825$ nm, $\lambda_{s,i} = 11650$ nm $\theta = 53.9^\circ$, $d_{\text{eff}} = 0.02$ pm/V	$\lambda_p = 4690$ nm, $\lambda_{s,i} = 9380$ nm $\theta = 49.8^\circ$, $d_{\text{eff}} = 0.02$ pm/V
TAS	$\lambda_p = 3620$ nm, $\lambda_{s,i} = 7240$ nm $\theta = 27.5^\circ$, $d_{\text{eff}} = 0.24$ pm/V	$\lambda_p = 5535$ nm, $\lambda_{s,i} = 11070$ nm $\theta = 27.0^\circ$, $d_{\text{eff}} = 0.23$ pm/V	$\lambda_p = 4570$ nm, $\lambda_{s,i} = 9140$ nm $\theta = 25.6^\circ$, $d_{\text{eff}} = 0.24$ pm/V
AGS	$\lambda_p = 1688$ nm, $\lambda_{s,i} = 3376$ nm $\theta = 53.7^\circ$, $d_{\text{eff}} = 0.14$ pm/V	$\lambda_p = 2845$ nm, $\lambda_{s,i} = 5690$ nm $\theta = 53.9^\circ$, $d_{\text{eff}} = 0.14$ pm/V	$\lambda_p = 2187$ nm, $\lambda_{s,i} = 4374$ nm $\theta = 48.9^\circ$, $d_{\text{eff}} = 0.15$ pm/V
AGSe	$\lambda_p = 2457$ nm, $\lambda_{s,i} = 4914$ nm $\theta = 79.9^\circ$, $d_{\text{eff}} = 0.11$ pm/V	$\lambda_p = 4079$ nm, $\lambda_{s,i} = 8158$ nm $\theta = 81.9^\circ$, $d_{\text{eff}} = 0.13$ pm/V	$\lambda_p = 3136$ nm, $\lambda_{s,i} = 6272$ nm $\theta = 67.2^\circ$, $d_{\text{eff}} = 0.25$ pm/V
GaSe	$\lambda_p = 2189$ nm, $\lambda_{s,i} = 4378$ nm $\theta = 16.1^\circ$, $d_{\text{eff}} = 0.51$ pm/V	$\lambda_p = 3657$ nm, $\lambda_{s,i} = 7314$ nm $\theta = 16.1^\circ$, $d_{\text{eff}} = 0.49$ pm/V	$\lambda_p = 2833$ nm, $\lambda_{s,i} = 5666$ nm $\theta = 15.0^\circ$, $d_{\text{eff}} = 0.51$ pm/V

bands. The corresponding spectral purity at $GVM_{1(2,3)}$ wavelengths is 0.97, 0.97, and 0.82, respectively.

For biaxial crystals, all the crystals we investigated can only satisfy the GVM conditions in the xy plane, with polar angle $\theta = 90^\circ$. We study 4 kinds of biaxial crystals and choose the LISe crystal as an example, which represents the mm2 point group. The assignment of dielectric and crystallographic axes are X, Y, Z ⇒ b, a, c. As shown in Figure 1(b), in the xy plane, the cross points reflect that the GVM condition can be fulfilled at the wavelength of 3,824, 6,410, and 4,982 nm, respectively.

Table 3: Three kinds of GVM conditions for 4 biaxial BPM crystals with light propagating in the xy plane. φ is the azimuth angle. d_{eff} is obtained from SNLO *v*78 [57].

Name	GVM_1 (purity ≈ 0.97)	GVM_2 (purity ≈ 0.97)	GVM_3 (purity ≈ 0.82)
LIS $-xy$	$\lambda_p = 1457$ nm, $\lambda_{s,i} = 2914$ nm $\varphi = 56.7^\circ$, $d_{\text{eff}} = 6.01$ pm/V	$\lambda_p = 2473$ nm, $\lambda_{s,i} = 4946$ nm $\varphi = 56.7^\circ$, $d_{\text{eff}} = 5.74$ pm/V	$\lambda_p = 1901$ nm, $\lambda_{s,i} = 3802$ nm $\varphi = 49.5^\circ$, $d_{\text{eff}} = 6.05$ pm/V
LISe $-xy$	$\lambda_p = 1912$ nm, $\lambda_{s,i} = 3824$ nm $\varphi = 45.8^\circ$, $d_{\text{eff}} = 9.65$ pm/V	$\lambda_p = 3205$ nm, $\lambda_{s,i} = 6410$ nm $\varphi = 45.6^\circ$, $d_{\text{eff}} = 9.31$ pm/V	$\lambda_p = 2491$ nm, $\lambda_{s,i} = 4982$ nm $\varphi = 40.7^\circ$, $d_{\text{eff}} = 9.19$ pm/V
LGS $-xy$	$\lambda_p = 1347$ nm, $\lambda_{s,i} = 2696$ nm $\varphi = 55.5^\circ$, $d_{\text{eff}} = 5.24$ pm/V	$\lambda_p = 2282$ nm, $\lambda_{s,i} = 4564$ nm $\varphi = 55.1^\circ$, $d_{\text{eff}} = 5.02$ pm/V	$\lambda_p = 1767$ nm, $\lambda_{s,i} = 3534$ nm $\varphi = 49.7^\circ$, $d_{\text{eff}} = 5.19$ pm/V
LGSe $-xy$	$\lambda_p = 1641$ nm, $\lambda_{s,i} = 3282$ nm $\varphi = 47.8^\circ$, $d_{\text{eff}} = 8.37$ pm/V	$\lambda_p = 2729$ nm, $\lambda_{s,i} = 5258$ nm $\varphi = 47.5^\circ$, $d_{\text{eff}} = 8.06$ pm/V	$\lambda_p = 2129$ nm, $\lambda_{s,i} = 4258$ nm $\varphi = 43.3^\circ$, $d_{\text{eff}} = 8.38$ pm/V

All the biaxial crystals can prepare pure-state in the range from 2,696 to 6,410 nm, as shown in Table 3. We can notice that the wavelength range is from 1,298 to 7,384 nm for the GVM_1 condition, from 2,312 to 11,650 nm for the GVM_2 condition, and from 1,658 to 9,380 nm for the GVM_3 condition (also shown in Figure 2), which can meet the different application demands in NIR, MIR, and telecom wavelengths.

3.2. Periodic Poling Crystals. In this section, we consider 8 periodic poling crystals with the QPM method, which has several advantages. For example, the largest component of the nonlinear coefficient matrix (usually d_{33}) can be utilized; there is no walk-off angle so as to achieve good spatial mode; it allows phase-matching interaction in isotropic media, in which the BPM is not applicable [59]. The GVM wavelengths, the poling period Λ, and the effective nonlinear coefficient d_{eff} are calculated and listed in Table 4. The LT, LN, KTP, and KN crystals are traditionally often-used QPM crystals [21, 60–62]. Here, we find that the GVM_2 wavelengths are all above 2 μm.

The $BaTiO_3$ crystal shows a low birefringence, thus, only suitable for the QPM method. With its high transmission in the IR range, it is possible to prepare pure-state at 3,036, 3,986, and 3,480 nm, respectively. The $MgBaF_4$ crystal can meet the GVM_1 condition at 1,978 nm and the GVM_3 condition at 2,780 nm. Note that this crystal does not satisfy the GVM_2 condition. The PMN-0.38PT is a functional ferroelectric material. The GVM condition only can be fulfilled at two wavelengths, i.e., 5,620 nm and 7,944 nm for GVM_1 and GVM_3 conditions. The orientation-patterned zinc selenide (OP–ZnSe) is an isotropic semiconductor material; therefore, the QPM rather than BPM is applicable. OP-ZnSe has extremely high nonlinear coefficients. Since the crystal possesses only one refractive index, it can only perform Type-0 SPDC, i.e., $e \longrightarrow e + e$ interaction, which will be discussed in the next section. All the QPM crystals can be prepared in the pure-state at the range from 1,224 to 7944 nm, as listed in Table 4.

3.3. Wavelength Nondegenerate Case. In this section, we focus on the wavelength nondegenerate case using the QPM method. Recently, we have investigated the wavelength nondegenerate case of doped PPLN crystal under type-0, type-I, and type-II conditions [24], and we utilize the same method to take OP-ZnSe as an example and calculate θ_{PMF} and the corresponding poling period Λ, as shown in Figure 3. The 50 curves with different colors in Figure 3(a) are based on equation (5) by changing $\tan(\theta_{\text{PMF}})$ from 0 to 90 degrees, and we depict 50 curves of the poling period Λ changing from 145 μm to 262 μm. The dashed black line in Figure 3 indicates the degenerate case, i.e., $2\lambda_p = \lambda_s$. For one fixed pump wavelength, we can find θ_{PMF} and Λ of different signal wavelengths.

The OP-ZnSe crystal can only perform Type-0 SPDC, i.e., $e \longrightarrow e + e$ interaction. Under the degenerate condition, the signal and the idler have the same group velocity, so the pure state cannot be prepared. The lines of all the angles θ_{PMF} converge in one point. At this point, all the GVM conditions are satisfied synchronously. Due to the singularity caused by these GVM conditions, the degenerate case at this point does not provide high purity, while the pure state can be prepared in the other area of different θ_{PMF}.

3.4. HOM Interference Simulation. The quality of the spectrally uncorrelated biphoton state can be tested by Hong-Ou-Mandel (HOM) interference. There are two kinds of HOM interference, the first one is the HOM interferences using signal and idler photons from the same SPDC source, with a typical setup, as shown in [63]. In this case, the two-fold coincidence probability $P_2(\tau)$ as a function of the time delay τ is given by [64–67] as follows:

$$P_2(\tau) = \frac{1}{4}\int_0^\infty \int_0^\infty d\omega_s d\omega_i \left| \left[f(\omega_s, \omega_i) - f(\omega_i, \omega_s) e^{-i(\omega_s - \omega_i)\tau} \right] \right|^2. \tag{11}$$

The second one is the HOM interference with two independent heralded single-photon sources, with a typical experimental setup, as shown in references [68–70]. In this interference, two signals s_1 and s_2 are sent to a beamsplitter for interference and two idlers i_1 and i_2 are detected by single-photon detectors for heralding the signals. The four-fold coincidence counts P_4 as a function of τ, which can be described by [65, 66] as follows:

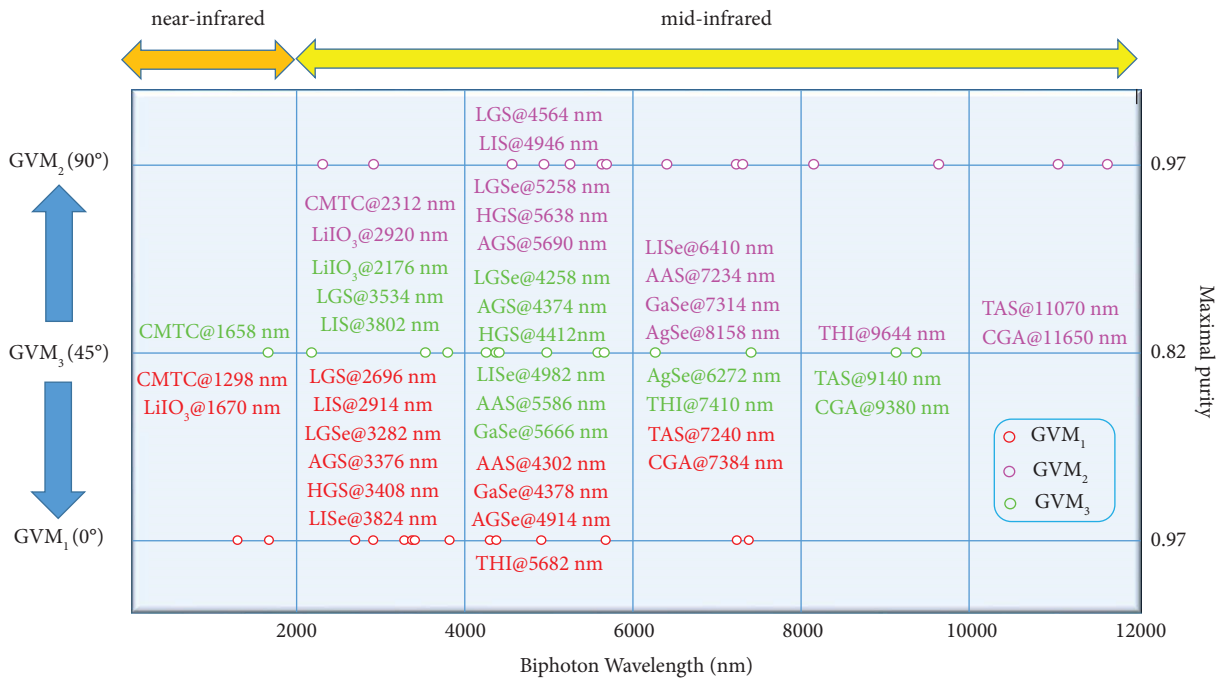

FIGURE 2: The result of all the BPM crystals for three kinds of GVM conditions. $GVM_{1(2)}$ can achieve a purity of 0.97. GVM_3 can achieve a purity of 0.82. The GVM angle increases from 0° to 45° and ends up at 90° on the left axis for $GVM_{1(2,3)}$ condition. The GVM_1 condition (red points) can cover the wavelength range from 1298 nm to 7384 nm. The GVM_2 condition (magenta points) can cover the wavelength range from 2312 nm to 11650 nm. The GVM_3 condition (green points) can cover the wavelength range from 1658 nm to 9380 nm.

TABLE 4: Three kinds of GVM conditions for 8 QPM crystals. $\lambda_{p(s,i)}$ is the GVM wavelength for the pump (signal, idler). Λ is the poling period, and d_{eff} is the effective nonlinear coefficient. The Sellmeier equations are obtained from refs. [34, 35]. Most of the d_{eff} values can be obtained from the SNLO *v*78 software package, developed by AS-Photonics, LLC [57]. *The d_{eff} values for $BaTiO_3$ and $MgBaF_4$ are not available from SNLO, so we have calculated them using the method in the appendix of ref. [52] and considering Miller's rule [58]. † The d_{eff} value for PMN-0.38PT is unknown.

Name	GVM_1 (purity ≈ 0.97)	GVM_2 (purity ≈ 0.97)	GVM_3 (purity ≈ 0.82)
LT	$\lambda_p = 1279$ nm, $\lambda_{s,i} = 2558$ nm $\Lambda = 33.7\ \mu$m, $d_{\text{eff}} = 0.27$ pm/V	$\lambda_p = 1320$ nm, $\lambda_{s,i} = 2640$ nm $\Lambda = 33.7\ \mu$m, $d_{\text{eff}} = 0.27$ pm/V	$\lambda_p = 1299$ nm, $\lambda_{s,i} = 2598$ nm $\Lambda = 33.7\ \mu$m, $d_{\text{eff}} = 0.27$ pm/V
LN	$\lambda_p = 1341$ nm, $\lambda_{s,i} = 2682$ nm $\Lambda = 14.7\ \mu$m, $d_{\text{eff}} = 2.70$ pm/V	$\lambda_p = 2015$ nm, $\lambda_{s,i} = 4030$ nm $\Lambda = 15.2\ \mu$m, $d_{\text{eff}} = 2.50$ pm/V	$\lambda_p = 1709$ nm, $\lambda_{s,i} = 3418$ nm $\Lambda = 15.5\ \mu$m, $d_{\text{eff}} = 2.60$ pm/V
KTP	$\lambda_p = 613$ nm, $\lambda_{s,i} = 1224$ nm $\Lambda = 70.2\ \mu$m, $d_{\text{eff}} = 2.50$ pm/V	$\lambda_p = 1169$ nm, $\lambda_{s,i} = 2338$ nm $\Lambda = 72.2\ \mu$m, $d_{\text{eff}} = 2.40$ pm/V	$\lambda_p = 792$ nm, $\lambda_{s,i} = 1584$ nm $\Lambda = 45.0\ \mu$m, $d_{\text{eff}} = 2.40$ pm/V
KN	$\lambda_p = 1412$ nm, $\lambda_{s,i} = 2824$ nm $\Lambda = 6.2\ \mu$m, $d_{\text{eff}} = 5.20$ pm/V	$\lambda_p = 1869$ nm, $\lambda_{s,i} = 3738$ nm $\Lambda = 6.1\ \mu$m, $d_{\text{eff}} = 5.00$ pm/V	$\lambda_p = 1605$ nm, $\lambda_{s,i} = 3210$ nm $\Lambda = 6.3\ \mu$m, $d_{\text{eff}} = 5.10$ pm/V
$BaTiO_3^*$	$\lambda_p = 1518$ nm, $\lambda_{s,i} = 3036$ nm $\Lambda = 23.3\ \mu$m, $d_{\text{eff}} = 10.13$ pm/V	$\lambda_p = 1993$ nm, $\lambda_{s,i} = 3986$ nm $\Lambda = 23.3\ \mu$m, $d_{\text{eff}} = 9.17$ pm/V	$\lambda_p = 1740$ nm, $\lambda_{s,i} = 3480$ nm $\Lambda = 23.8\ \mu$m, $d_{\text{eff}} = 9.69$ pm/V
$MgBaF_4^*$	$\lambda_p = 989$ nm, $\lambda_{s,i} = 1978$ nm $\Lambda = 948.5\ \mu$m, $d_{\text{eff}} = 0.04$ pm/V	Not satisfied	$\lambda_p = 1390$ nm, $\lambda_{s,i} = 2780$ nm $\Lambda = 680.6\ \mu$m, $d_{\text{eff}} = 0.04$ pm/V
PMN-0.38PT†	$\lambda_p = 2810$ nm, $\lambda_{s,i} = 5620$ nm $\Lambda = 1301.38\ \mu$m, $d_{\text{eff}} =$ unknown	Not satisfied	$\lambda_p = 3972$ nm, $\lambda_{s,i} = 7944$ nm $\Lambda = 917.83\ \mu$m, $d_{\text{eff}} =$ unknown
OP-ZnSe		$\lambda_p = 3403$ nm, $\lambda_{s,i} = 6806$ nm $\Lambda = 262.97\ \mu$m, $d_{\text{eff}} = 19.1$ pm/V	

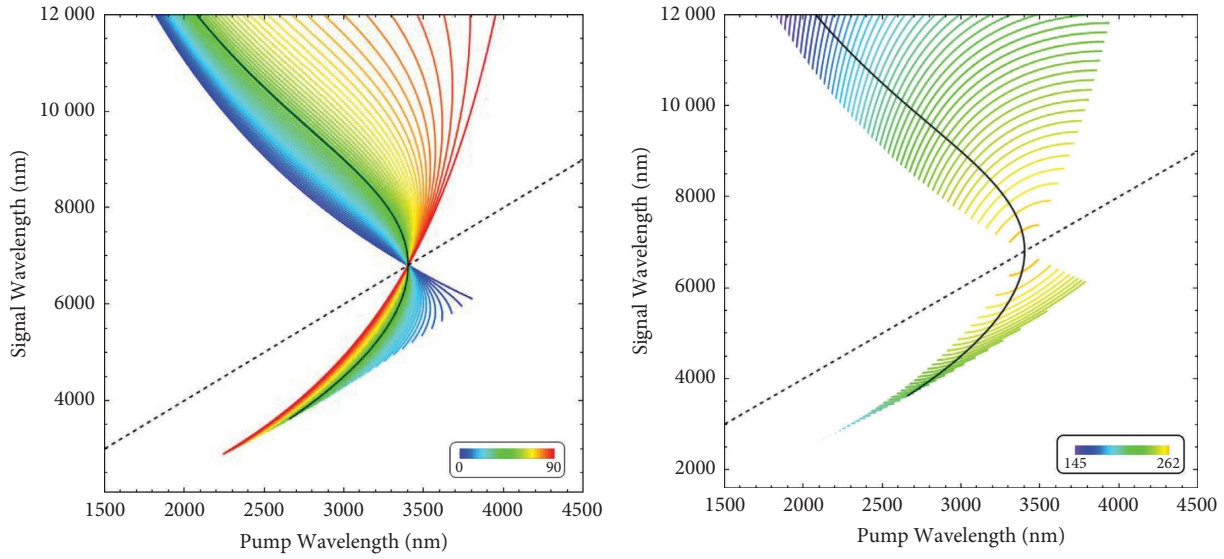

FIGURE 3: (a, b): The GVM angle θ_{PMF} and the corresponding poling period Λ for QPM crystal OP-ZnSe. The solid black line indicates $\theta_{\mathrm{PMF}} = 45°$, and the dashed black line indicates the degenerate case $2\lambda_p = \lambda_s$. In this figure, the QPM nondegenerate wavelengths' case is under type-0 phase-matching condition. (a) ZnSe-θ (°). (b) ZnSe-Λ (μm).

$$P_4(\tau) = \frac{1}{4}\int_0^\infty \int_0^\infty \int_0^\infty \int_0^\infty d\omega_{s_1} d\omega_{s_2} d\omega_{i_1} d\omega_{i_2} \left| f_1(\omega_{s_1}, \omega_{i_1}) f_2(\omega_{s_2}, \omega_{i_2}) - f_1(\omega_{s_2}, \omega_{i_1}) f_2(\omega_{s_1}, \omega_{i_2}) e^{-i(\omega_{s_2} - \omega_{s_1})\tau} \right|^2, \tag{12}$$

where f_1 and f_2 are the JSAs from the first and the second crystals.

We chose $BiTaO_3$, LGSe, and PMN-0.38PT as examples to test the HOM interference. Figure 4(a) shows that JSA is generated from $BiTaO_3$ crystal, which is under the GVM_1 condition. $BiTaO_3$ crystal is a uniaxial QPM crystal. The JSA is obtained by using a pump laser with a bandwidth of $\Delta\lambda = 4$ nm and a crystal length L of 100 mm. The JSA has a long stripe shape along the horizontal axis. Considering the spectral distributions of the signal and the idler photons, we can obtain them by projecting the joint spectral intensity onto the horizontal and vertical axes. The FWHM of the signal (idler) is 27.02 nm (0.92 nm). Figure 4(c) shows the HOM pattern of two signals heralded by two idlers; the FWHM is 726.87 fs with a visibility of 96.68%. Figure 4(d) shows the HOM pattern of two heralded idlers with an FWHM of 8.74 ps and a visibility of 96.68%.

For the GVM_2 condition, the result is on the second row of Figure 4. We investigate a biaxial BPM crystal LGSe. The JSA shape is also a long stripe, but it is located along the vertical axis. The pump bandwidth $\Delta\lambda$ and the crystal length L of Figure 4(e) are 8 nm and 200 mm. The FWHM of the signal (idler) is 5.17 nm (75.40 nm) for Figure 4(f). The FWHM of the HOM pattern by two heralded signals (idler) is 12.46 ps (1.17 ps), and the visibility is 97.05%, as shown in Figures 4(g) and 4(h).

For the GVM_3 condition, the result is on the third row of Figure 4. We concentrate on the PMN-0.38PT crystal. This crystal has been studied before; however, it only focuses on the GVM_1 and GVM_2 conditions [22]. Here, we make a thorough study of the GVM_3 condition. In this case, the JSA shape is near-round and the spectra of the signal and idler are almost equal. Figure 4(i) is obtained by using a pump bandwidth of $\Delta\lambda = 11$ nm and a crystal length L of 100 mm. The spectra of the signal and idler have the same FWHM of 54.64 nm. The HOM interference from two independent signal or idler sources manifests the same performance with the FWHM of 12.24 ps and visibility of 82.33%, which is much lower than the GVM_1 and GVM_2 cases. In case of the two-fold HOM interference, the visibility is 100% and the FWHM of the HOM pattern is 2.20 ps for Figure 4(l).

4. Discussion

We summarize the result of all the BPM crystals in Figure 2. The left vertical axis of the figure denotes the GVM condition and the corresponding PMF angle θ_{PMF}. The right vertical axis shows the maximal purity. The horizontal axis shows a wavelength range from 0 to 12 μm. Most of the crystals are located on the MIR band, from 2 μm to 12 μm. There are three cases on the NIR band. We also conclude the results of QPM crystals in Figure 5, which shows the down-converted wavelength, the poling period, and the maximal purity for all the results we calculated above.

It is important to discuss the detection of single photons in the MIR region. Recent work shows that superconducting nanowire single-photon detectors (SNSPD), which have the

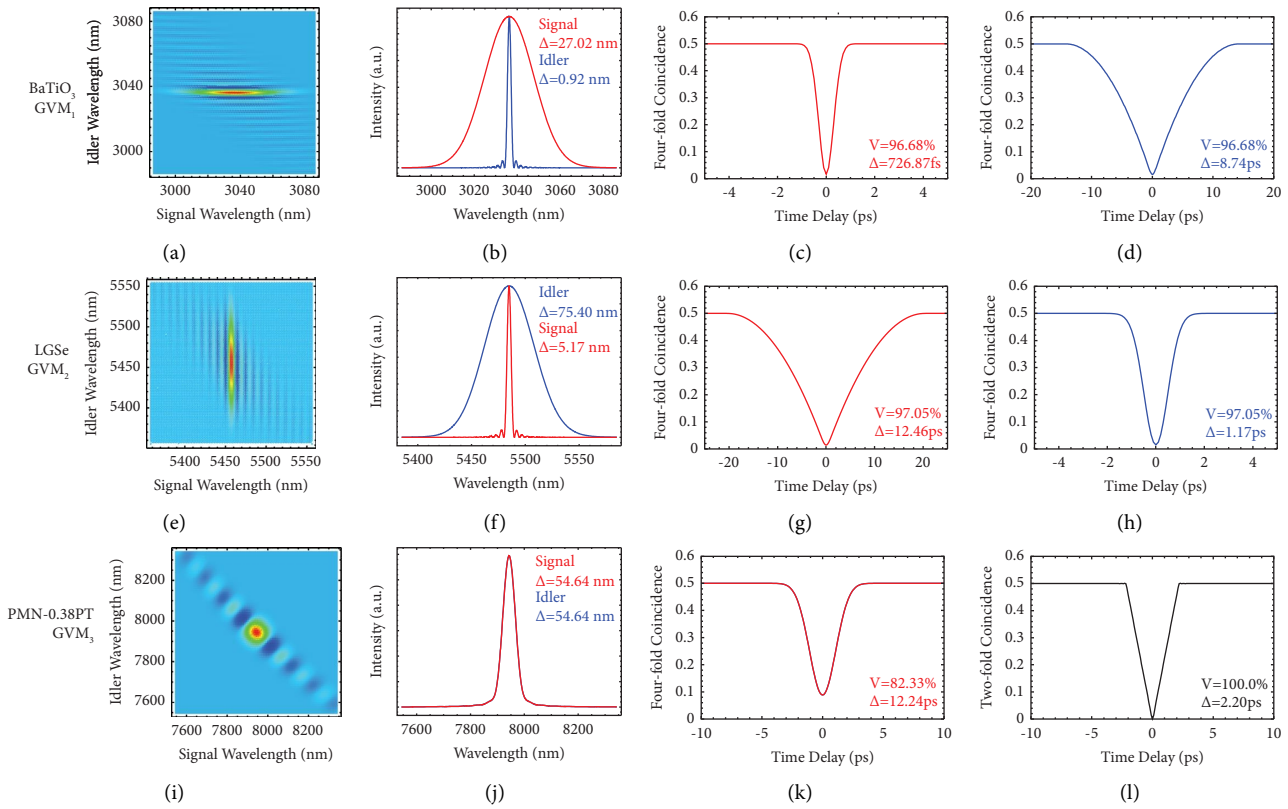

FIGURE 4: (a, e, i) are the JSAs; (b, f, j) are the spectra; and (c, d, g, h, k, l) are the HOM interference patterns. The FWHM of the spectra (Δ) for the signal and the idler, the visibility (V), and the FWHM (Δ) of two-fold and four-fold HOM interference are shown in the figures. The parameters of $L = 100\,\text{mm}$ and $\Delta\lambda = 4\,\text{nm}$ (FWHM = 6.66 nm), $L = 200\,\text{mm}$ and $\Delta\lambda = 8\,\text{nm}$ (FWHM = 13.32 nm), $L = 100\,\text{mm}$ and $\Delta\lambda = 11\,\text{nm}$ (FWHM = 18.32 nm) are adopted for $BaTiO_3$, LGSe, and PMN-0.38PT, respectively. Note that for all the calculations of purity, we use a grid size of 200×200 for all the JSAs.

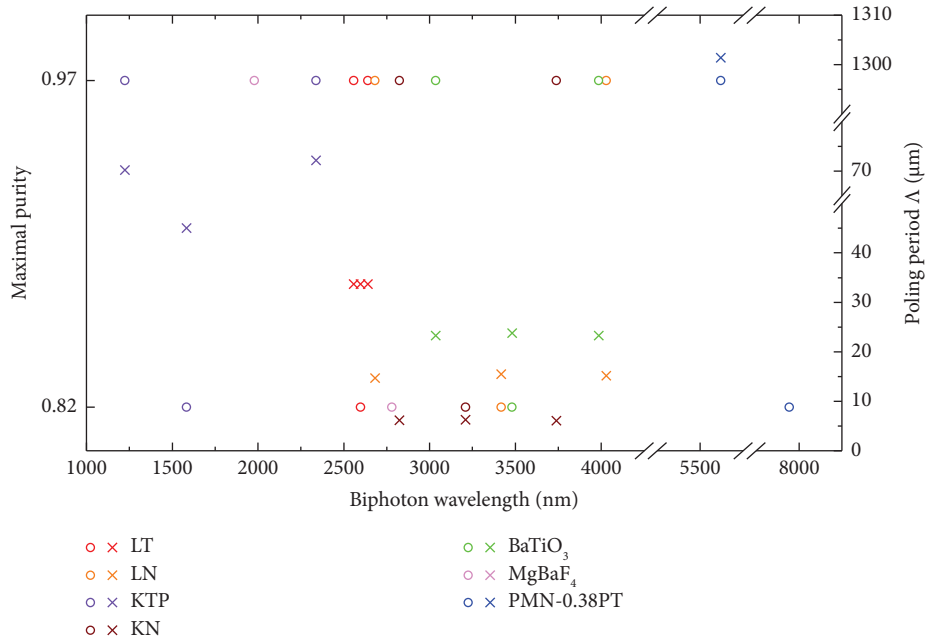

FIGURE 5: The result of all the QPM crystals for three kinds of GVM conditions. $GVM_{1\,(2)}$ can achieve a purity of 0.97. GVM_3 can achieve a purity of 0.82. The wavelength versus achievable maximal spectral purity and poling period Λ can be reflected on the scale of the left and right Y-axis. The wavelength range is from 1,224 nm to 7,944 nm, and the poling period Λ is from 6.1 μm to 1,301.38 μm.

best performance (98%) in the NIR band [71], while having a detection efficiency at MIR band of 70% at 2 μm [72], 40% at 2.5 μm and 10% at 3 μm [73], and 1.64% for free-space communication [30]; upconversion detectors module combined with the SAPD method demonstrates the efficiency of 6.5% at room temperature [14]; semiconductor photodiodes such as Cd admixture, graphene, black arsenic phosphorus, black phosphorus carbide, tellurene, $PtSe_2$, and $PdSe_2$ are good candidates for wide detection range [74]. A recent review about MIR single-photon detection is presented in [75]. In the future, developing new material for SNSPD and a more effective nonlinear process of upconversion for MIR detection will be promising [76].

Except for the 22 crystals discussed above, we still find 6 kinds of new crystals in the MIR band, which are as follows: BGS, BGSe, BGGS, BGGSe, BGSS, and BGSSe [77–81]. They can be written as $BaGa_4X_7$ (X = S, Se) and $BaGa_2MX_6$ (M = Si, Ge; X = S, Se). Since the d_{eff} calculated and phase-matched methods of these crystals are complex [82–86], we did not discuss them in this work. d_{eff} for BGS and BGSe has been investigated in [87]. d_{33} for BGGS, BGGSe, BGSS, and BGSSe is −12.0, −23.0, 8.4, and 12.3 pm/V, respectively [88]. Moreover, the doping method can be utilized as a degree of freedom to manipulate the single-photon state at the MIR range [24].

For the GVM_3 condition, the purity can be further improved from 0.82 to near 1 using the custom poling crystal scheme, for example, by applying the machine learning method or metaheuristic algorithm [25, 89].

5. Conclusion

In conclusion, we have theoretically investigated 22 nonlinear optical crystals for MIR photon generation. The down-converted photons' wavelength ranges from 1,298 nm (1,224 nm) to 11,650 nm (7,944 nm) for the BPM (QPM) crystals. The corresponding purity for the three kinds of GVM conditions is around 0.97, 0.97, and 0.82, respectively. The wavelength nondegenerated condition, the 4-fold HOM interference, and the 2-fold HOM interference are calculated in detail. This research study may be helpful in the study of quantum communication, quantum imaging, and quantum metrology at the MIR range.

Data Availability

The data used to support the findings of this study are available from the corresponding author upon reasonable request.

Disclosure

The preprint has previously been published [90].

Conflicts of Interest

The authors declare that they have no conflicts of interest.

Acknowledgments

We thank Prof. Keiichi Edamatsu for the helpful discussions. This work was supported by the National Natural Science Foundations of China (Grant no. 12074299), the Natural Science Foundation of Hubei Province (Grant no. 2022CFA039), and the JST SPRING (Grant no. JPMJSP2114).

References

[1] M. Ebrahim-Zadeh and I. T. Sorokina, *Mid-Infrared Coherent Sources and Applications*, Springer Science and Business Media, Berlin, Germany, 2008.

[2] E. Tournie and L. Cerutti, *Mid-infrared Optoelectronics Materials, Devices, and Applications*, Woodhead Publishing, Sawston, UK, 2019.

[3] I. A. Walmsley and M. G. Raymer, "Toward quantum-information processing with photons," *Science*, vol. 307, no. 5716, pp. 1733-1734, 2005.

[4] S. Slussarenko and G. J. Pryde, "Photonic quantum information processing: a concise review," *Applied Physics Reviews*, vol. 6, no. 4, 2019.

[5] D. Caffey, M. B. Radunsky, and V. Cook, "Recent results from broadly tunable external cavity quantum cascade lasers," in *Novel In-Plane Semiconductor Lasers X. 7953*, A. A. Belyanin and P. M. Smowton, Eds., International Society for Optics and Photonics. SPIE, Washington, DC, USApp. 336–346, 2011.

[6] R. S. El Shamy, D. Khalil, and M. A. Swillam, "Mid infrared optical gas sensor using plasmonic mach-zehnder interferometer," *Scientific Reports*, vol. 10, no. 1, Article ID 1293, 2020.

[7] K. Chen, S. Liu, B. Zhang et al., "Highly sensitive photoacoustic multi-gas analyzer combined with mid-infrared broadband source and near-infrared laser," *Optics and Lasers in Engineering*, vol. 124, Article ID 105844, 2020.

[8] L. Høgstedt, J. S. Dam, A. L. Sahlberg et al., "Low-noise mid-IR upconversion detector for improved IR-degenerate four-wave mixing gas sensing," *Optics Letters*, vol. 39, no. 18, pp. 5321–5324, 2014.

[9] G. J. Edelman, R. J. Hoveling, M. Roos, T. G. van Leeuwen, and M. C. Aalders, "Infrared imaging of the crime scene: possibilities and pitfalls," *Journal of Forensic Sciences*, vol. 58, no. 5, pp. 1156–1162, 2013.

[10] J. Shi, T. T. W. Wong, Y. He et al., "High-resolution, high-contrast mid-infrared imaging of fresh biological samples with ultraviolet-localized photoacoustic microscopy," *Nature Photonics*, vol. 13, no. 9, pp. 609–615, 2019.

[11] J. Yin, Y. Cao, Y. H. Li et al., "Satellite-based entanglement distribution over 1200 kilometers," *Science*, vol. 356, no. 6343, pp. 1140–1144, 2017.

[12] S. Wang, Z. Q. Yin, D. Y. He et al., "Twin-field quantum key distribution over 830-km fibre," *Nature Photonics*, vol. 16, no. 2, pp. 154–161, 2022.

[13] L. Zhou, Y. B. Sheng, and G. L. Long, "Device-independent quantum secure direct communication against collective attacks," *Science Bulletin*, vol. 65, no. 1, pp. 12–20, 2020.

[14] M. Mancinelli, A. Trenti, S. Piccione et al., "Mid-infrared coincidence measurements on twin photons at room temperature," *Nature Communications*, vol. 8, no. 1, Article ID 15184, 2017.

[15] Y. M. Sua, H. Fan, A. Shahverdi, J. Y. Chen, and Y. P. Huang, "Direct Generation and Detection of Quantum Correlated Photons with 3.2 um Wavelength Spacing," *Scientific Reports*, vol. 7, no. 1, Article ID 17494, 2017.

[16] M. Arahata, Y. Mukai, B. Cao, T. Tashima, R. Okamoto, and S. Takeuchi, "Wavelength variable generation and detection of photon pairs in visible and mid-infrared regions via spontaneous parametric downconversion," *Journal of the Optical Society of America B*, vol. 38, no. 6, pp. 1934–1941, 2021.

[17] P. S. Kuo, P. G. Schunemann, and M. V. Camp, "Towards a source of entangled photon pairs in gallium phosphide," in *Optical Society of America*, Optica Publishing Group, Washington, DC, USA, 2019.

[18] L. M. Rosenfeld, D. A. Sulway, G. F. Sinclair et al., "Mid-infrared quantum optics in silicon," *Optics Express*, vol. 28, no. 25, pp. 37092–37102, 2020.

[19] S. Prabhakar, T. Shields, A. C. Dada et al., "Two-photon quantum interference and entanglement at 2.1 μm," *Science Advances*, vol. 6, no. 13, Article ID eaay5195, 2020.

[20] M. Hojo and K. Tanaka, "Broadband infrared light source by simultaneous parametric down-conversion," *Scientific Reports*, vol. 11, no. 1, Article ID 17986, 2021.

[21] K. J. Lee, S. Lee, and H. Shin, "Extended phase-matching properties of periodically poled potassium niobate crystals for mid-infrared polarization-entangled photon-pair generation," *Applied Optics*, vol. 55, no. 34, pp. 9791–9796, 2016.

[22] D. Kundys, F. Graffitti, R. A. McCracken, A. Fedrizzi, and B. Kundys, "Numerical study of reconfigurable mid-IR single photon sources based on functional ferroelectrics," *Advanced Quantum Technologies*, vol. 3, no. 3, Article ID 1900092, 2020.

[23] R. A. McCracken, F. Graffitti, and A. Fedrizzi, "Numerical investigation of mid-infrared single-photon generation," *Journal of the Optical Society of America B*, vol. 35, no. 12, pp. C38–C48, 2018.

[24] B. Wei, W. H. Cai, C. Ding et al., "Mid-infrared spectrally-uncorrelated biphotons generation from doped PPLN: a theoretical investigation," *Optics Express*, vol. 29, no. 1, pp. 256–271, 2021.

[25] W. H. Cai, Y. Tian, S. Wang, C. You, Q. Zhou, and R. B. Jin, "Optimized design of the lithium niobate for spectrally-pure-state generation at MIR wavelengths using metaheuristic algorithm," *Advanced Quantum Technologies*, vol. 5, no. 7, Article ID 2200028, 2022.

[26] J. L. Zhu, W. X. Zhu, X. T. Shi et al., "Design of mid-infrared entangled photon sources using lithium niobate," *Journal of the Optical Society of America B*, vol. 40, no. 1, p. A9, 2023.

[27] C. T. Zhang, X. T. Shi, W. X. Zhu, J. L. Zhu, X. Y. Hao, and R. B. Jin, "Preparation of spectrally pure single-photon source at 3 μm mid-infrared band from lithium niobate crystal with domain sequence algorithm," *Acta Physica Sinica*, vol. 71, no. 20, Article ID 204201, 2022.

[28] R. Razali, Z. Ikonić, D. Indjin, and P. Harrison, "Polarization-entangled mid-infrared photon generation inp-doped semiconductor quantum wells," *Semiconductor Science and Technology*, vol. 31, no. 11, Article ID 115011, 2016.

[29] F. Marsili, F. Bellei, F. Najafi et al., "Efficient single photon detection from 500 nm to 5 μm wavelength," *Nano Letters*, vol. 12, no. 9, pp. 4799–4804, 2012.

[30] F. Bellei, A. P. Cartwright, A. N. McCaughan et al., "Free-space-coupled superconducting nanowire single-photon detectors for infrared optical communications," *Optics Express*, vol. 24, no. 4, pp. 3248–3257, 2016.

[31] P. S. Kuo, "Using silica fiber coupling to extend superconducting nanowire single-photon detectors into the infrared," *OSA Continuum*, vol. 1, no. 4, pp. 1260–1266, 2018.

[32] S. Piccione, M. Mancinelli, A. Trenti, K. L. Vodopyanov, and K. L. Schepler, "Mid-infrared coincidence measurements based on intracavity frequency conversion," in *Nonlinear Frequency Generation And Conversion: Materials And Devices XVII. 10516*, pp. 251–258, International Society for Optics and Photonics. SPIE, New, York, NY, USA, 2018.

[33] W. P. Grice, A. B. U'Ren, and I. A. Walmsley, "Eliminating frequency and space-time correlations in multiphoton states," *Physical Review A*, vol. 64, no. 6, Article ID 063815, 2001.

[34] V. G. Dmitriev, G. G. Gurzadyan, and D. N. Nikogosyan, *Handbook of Nonlinear Optical Crystals*, Springer-Verlag, Berlin, Germany, 3rd edition, 1999.

[35] D. N. Nikogosyan, *Nonlinear Optical Crystals: A Complete Survey*, Springer-Verlag, Berlin, Germany, 2005.

[36] F. Wang, "Calculation of the electro-optical and nonlinear optical coefficients of ferroelectric materials from their linear properties," *Physical Review B: Condensed Matter*, vol. 59, pp. 9733–9736, 1999.

[37] K. Kato, "High-power difference-frequency generation at 4.4-5.7 μm in $LiIO_3$," *IEEE Journal of Quantum Electronics*, vol. 21, no. 2, pp. 119-120, 1985.

[38] K. Kato, V. Petrov, and N. Umemura, "Phase-matching properties of yellow color $HgGa_2S_4$ for SHG and SFG in the 0.944–10.5910 μm range," *Applied Optics*, vol. 55, no. 12, pp. 3145–3148, 2016.

[39] G. C. Bhar, "Refractive index interpolation in phase-matching," *Applied Optics*, vol. 15, no. 2, pp. 305_1–307, 1976.

[40] K. Kato, F. Tanno, and N. Umemura, "Sellmeier and thermo-optic dispersion formulas for GaSe (Revisited)," *Applied Optics*, vol. 52, no. 11, pp. 2325–2328, 2013.

[41] S. Fossier, S. Salaün, and J. Mangin, "Optical, vibrational, thermal, electrical, damage, and phase-matching properties of lithium thioindate," *Journal of the Optical Society of America B*, vol. 21, no. 11, pp. 1981–2007, 2004.

[42] K. Kato, V. Petrov, and N. Umemura, "Sellmeier and thermo-optic dispersion formulas for $LiInSe_2$," *Applied Optics*, vol. 53, no. 6, pp. 1063–1066, 2014.

[43] V. Petrov, J. J. Zondy, and O. Bidault, "Optical, thermal, electrical, damage, and phase-matching properties of lithium selenoindate," *Journal of the Optical Society of America B*, vol. 27, no. 9, pp. 1902–1927, 2010.

[44] K. Kato, K. Miyata, L. Isaenko, S. Lobanov, V. Vedenyapin, and V. Petrov, "Phase-matching properties of $LiGaS_2$ in the 1.025–10.5910 μm spectral range," *Optics Letters*, vol. 42, no. 21, pp. 4363–4366, 2017.

[45] V. Petrov, A. Yelisseyev, L. Isaenko, S. Lobanov, A. Titov, and J. J. Zondy, "Second harmonic generation and optical parametric amplification in the mid-IR with orthorhombic biaxial crystals $LiGaS_2$ and $LiGaSe_2$," *Applied Physics B*, vol. 78, no. 5, pp. 543–546, 2004.

[46] K. Miyata, V. Petrov, and K. Kato, "Phase-matching properties of $LiGaSe_2$ for SHG and SFG in the 1.026–10.5910 μm range," *Applied Optics*, vol. 56, no. 22, pp. 6126–6129, 2017.

[47] I. Dolev, A. Ganany-Padowicz, O. Gayer, A. Arie, J. Mangin, and G. Gadret, "Linear and nonlinear optical properties of $MgO:LiTaO_3$," *Applied Physics B*, vol. 96, no. 2-3, pp. 423–432, 2009.

[48] M. V. Pack, D. J. Armstrong, and A. V. Smith, "Measurement of the $\chi^{(2)}$ tensor of the potassium niobate crystal," *Journal of the Optical Society of America B*, vol. 20, no. 10, pp. 2109–2116, 2003.

[49] C. He, W. Ge, X. Zhao, H. Xu, H. Luo, and Z. Zhou, "Wavelength dependence of electro-optic effect in tetragonal lead magnesium niobate lead titanate single crystals," *Journal of Applied Physics*, vol. 100, no. 11, Article ID 113119, 2006.

[50] W. J. Tropf, "Temperature-dependent refractive index models for BaF_2, CaF_2, MgF_2, SrF_2, LiF, NaF, KCl, ZnS, and ZnSe," *Optical Engineering*, vol. 34, no. 5, pp. 1369–1373, 1995.

[51] P. J. Mosley, J. S. Lundeen, B. J. Smith, and I. A. Walmsley, "Conditional preparation of single photons using parametric downconversion: a recipe for purity," *New Journal of Physics*, vol. 10, no. 9, Article ID 093011, 2008.

[52] R. B. Jin, W. H. Cai, C. Ding et al., "Spectrally uncorrelated biphotons generated from "the family of BBO crystal"," *Quantum Engineering*, vol. 2, no. 2, Article ID e38, 2020.

[53] R. B. Jin, R. Shimizu, K. Wakui, H. Benichi, and M. Sasaki, "Widely tunable single photon source with high purity at telecom wavelength," *Optics Express*, vol. 21, no. 9, pp. 10659–10666, 2013.

[54] R. B. Jin, N. Cai, Y. Huang et al., "Theoretical investigation of a spectrally pure-state generation from isomorphs of KDP crystal at near-infrared and telecom wavelengths," *Physical Review Applied*, vol. 11, no. 3, Article ID 034067, 2019.

[55] F. Graffitti, J. Kelly-Massicotte, A. Fedrizzi, and A. M. Branczyk, "Design considerations for high-purity heralded single-photon sources," *Physical Review A*, vol. 98, no. 5, Article ID 053811, 2018.

[56] N. Quesada and A. M. Brańczyk, "Gaussian functions are optimal for waveguided nonlinear-quantum-optical processes," *Physical Review A*, vol. 98, no. 4, Article ID 043813, 2018.

[57] A. Smith, "SNLO," 2023, http://www.as-photonics.com/snlo.

[58] A. V. Smith, *Crystal Nonlinear Optics: With SNLO Examples*, AS-Photonics, Albuquerque, NM, USA, 2018.

[59] D. S. Hum and M. M. Fejer, "Quasi-phase-matching," *Comptes Rendus Physique*, vol. 8, no. 2, pp. 180–198, 2007.

[60] R. Shimizu and K. Edamatsu, "High-flux and broadband biphoton sources with controlled frequency entanglement," *Optics Express*, vol. 17, no. 19, pp. 16385–16393, 2009.

[61] T. Wang, P. Chen, C. Xu et al., "Periodically poled $LiNbO_3$ crystals from 1D and 2D to 3D," *Science China Technological Sciences*, vol. 63, no. 7, pp. 1110–1126, 2020.

[62] R. B. Jin, P. Zhao, P. Deng, and Q. L. Wu, "Spectrally pure states at telecommunications wavelengths from periodically poled $MTiOXO_4$(M = K, Rb, Cs; X = P, As) crystals," *Physical Review Applied*, vol. 6, no. 6, Article ID 064017, 2016.

[63] C. K. Hong, Z. Y. Ou, and L. Mandel, "Measurement of subpicosecond time intervals between two photons by interference," *Physical Review Letters*, vol. 59, no. 18, pp. 2044–2046, 1987.

[64] W. P. Grice and I. A. Walmsley, "Spectral information and distinguishability in type-II down-conversion with a broadband pump," *Physical Review A*, vol. 56, no. 2, pp. 1627–1634, 1997.

[65] Z. Y. J. Ou, *Multi-Photon Quantum Interference*, Springer, Berlin, Germany, 2007.

[66] R. B. Jin, T. Gerrits, M. Fujiwara et al., "Spectrally resolved Hong-Ou-Mandel interference between independent photon sources," *Optics Express*, vol. 23, no. 22, pp. 28836–28848, 2015.

[67] Y. Tian, W. H. Cai, Z. X. Yang, F. Chen, R. B. Jin, and Q. Zhou, "Hong-Ou-Mandel interference of entangled photons generated under pump-tight-focusing condition," *Acta Physica Sinica*, vol. 71, no. 5, Article ID 054201, 2022.

[68] P. J. Mosley, J. S. Lundeen, B. J. Smith et al., "Heralded generation of ultrafast single photons in pure quantum states," *Physical Review Letters*, vol. 100, no. 13, Article ID 133601, 2008.

[69] R. B. Jin, K. Wakui, R. Shimizu et al., "Nonclassical interference between independent intrinsically pure single photons at telecommunication wavelength," *Physical Review A*, vol. 87, no. 6, Article ID 063801, 2013.

[70] A. Xu, L. Duan, L. Wang, and Y. Zhang, "Characterization of two-photon interference between a weak coherent state and a heralded single photon state," *Optics Express*, vol. 31, no. 4, pp. 5662–5669, 2023.

[71] D. V. Reddy, R. R. Nerem, S. W. Nam, R. P. Mirin, and V. B. Verma, "Superconducting nanowire single-photon detectors with 98% system detection efficiency at 1550 nm," *Optica*, vol. 7, no. 12, pp. 1649–1653, 2020.

[72] J. Chang, J. W. N. Los, R. Gourgues et al., "Efficient mid-infrared single-photon detection using superconducting NbTiN nanowires with high time resolution in a Gifford-McMahon cryocooler," *Photonics Research*, vol. 10, no. 4, pp. 1063–1070, 2022.

[73] P. I. Zolotov, A. V. Divochiy, Y. B. Vakhtomin, P. V. Morozov, V. A. Seleznev, and K. V. Smirnov, "Development of high-effective superconducting single-photon detectors aimed for mid-IR spectrum range," *Journal of Physics: Conference Series*, vol. 917, Article ID 062037, 2017.

[74] M. Long, P. Wang, H. Fang, and W. Hu, "Progress, challenges, and opportunities for 2D material based photodetectors," *Advanced Functional Materials*, vol. 29, no. 19, Article ID 1803807, 2018.

[75] S. Dello Russo, A. Elefante, D. Dequal et al., "Advances in mid-infrared single-photon detection," *Photonics*, vol. 9, no. 7, p. 470, 2022.

[76] R. B. Jin and Y. Tian, "Research progress on the mid-infrared band quantum light source," *Journal of Anhui University (Natural Science Edition)*, vol. 45, no. 5, pp. 10–19, 2022.

[77] X. Li, C. Li, P. Gong, Z. Lin, J. Yao, and Y. Wu, "$BaGa_2$ $SnSe_6$: a new phase-matchable IR nonlinear optical material with strong second harmonic generation response," *Journal of Materials Chemistry C: Materials for Optical and Electronic Devices*, vol. 3, no. 42, pp. 10998–11004, 2015.

[78] N. Zhai, C. Li, B. Xu et al., "Temperature-dependent Sellmeier equations of IR nonlinear optical crystal $BaGa_4Se_7$," *Crystals*, vol. 7, no. 3, p. 62, 2017.

[79] Y. He, Y. Guo, D. Xu et al., "High energy and tunable mid-infrared source based on $BaGa_4Se_7$ crystal by single-pass difference-frequency generation," *Optics Express*, vol. 27, no. 6, pp. 9241–9249, 2019.

[80] K. Kato, V. V. Badikov, L. Wang et al., "Effective nonlinearity of the new quaternary chalcogenide crystal $Baga_2GeSe_6$," *Optics Letters*, vol. 45, no. 8, pp. 2136–2139, 2020.

[81] U. Elu, L. Maidment, L. Vamos et al., "Few-cycle mid-infrared pulses from $Baga_2GeSe_6$," *Optics Letters*, vol. 45, no. 13, pp. 3813–3815, 2020.

[82] E. Boursier, P. Segonds, J. Debray et al., "Angle noncritical phase-matched second-harmonic generation in the monoclinic crystal $BaGa_4Se_7$," *Optics Letters*, vol. 40, no. 20, pp. 4591–4594, 2015.

[83] E. Boursier, P. Segonds, B. Ménaert et al., "Phase-matching directions and refined Sellmeier equations of the monoclinic acentric crystal $BaGa_4$ Se_7," *Optics Letters*, vol. 41, no. 12, pp. 2731–2734, 2016.

[84] K. Kato, K. Miyata, and V. Petrov, "Phase-matching properties of $BaGa_4Se_7$ for SHG and SFG in the 0.901–10.5910 μm range," *Applied Optics*, vol. 56, no. 11, pp. 2978–2981, 2017.

[85] K. Kato, K. Miyata, V. V. Badikov, and V. Petrov, "Phase-matching properties of $BaGa_2GeSe_6$ for three-wave interactions in the 0.778–10.5910 μm spectral range," *Applied Optics*, vol. 57, no. 26, pp. 7440–7443, 2018.

[86] P. Liu, L. Guo, F. Qi et al., "Large dynamic range and wideband mid-infrared upconversion detection with $BaGa_4Se_7$ crystal," *Optica*, vol. 9, no. 1, pp. 50–55, 2022.

[87] V. Badikov, D. Badikov, and G. Shevyrdyaeva, "Phase-matching properties of $Baga_4S_7$ and $Baga_4Se_7$: wide-bandgap nonlinear crystals for the mid-infrared," in *Optical Society of America*, Optica Publishing Group, Washington, DC, USA, 2011.

[88] W. Yin, K. Feng, R. He et al., "$BaGa_2MQ_6$ (M= Si, Ge; Q= S, Se): a new series of promising IR nonlinear optical materials," *Dalton Transactions*, vol. 41, no. 18, pp. 5653–5661, 2012.

[89] C. Cui, R. Arian, S. Guha, N. Peyghambarian, Q. Zhuang, and Z. Zhang, "Wave-function engineering for spectrally uncorrelated biphotons in the telecommunication band based on a machine-learning framework," *Physical Review Applied*, vol. 12, no. 3, Article ID 034059, 2019.

[90] W. H. Cai, Y. Tian, and R. B. Jin, "Mid-infrared spectrally-pure single-photon states generation from 22 nonlinear optical crystals," 2023, https://arxiv.org/abs/2303.13106.